

Spin fluctuations and orbital-selective superconductivity in Ba_2CuO_{4-y}: A FLEX study

Pei-Jun Zheng(郑裴俊), Ya-Min Quan(全亚民), and Liang-Jian Zou(邹良剑)
Citation: Chin. Phys. B, 2024, 33 (**12**): 127401. DOI: 10.1088/1674-1056/ad8cbe
Journal homepage: http://cpb.iphy.ac.cn; http://iopscience.iop.org/cpb

What follows is a list of articles you may be interested in

Effects of carrier density and interactions on pairing symmetry in a t_{2g} model

Yun-Xiao Li(李云霄), Wen-Han Xi(西文翰), Zhao-Yang Dong(董召阳), Zi-Jian Yao(姚子健), Shun-Li Yu(于顺利), and Jian-Xin Li(李建新)
Chin. Phys. B, 2024, 33 (**1**): 017404. DOI: 10.1088/1674-1056/ad1094

Role of grain boundary networks in vortex motion in superconducting films

Yu Liu(刘宇), Feng Xue(薛峰), and Xiao-Fan Gou(苟晓凡)
Chin. Phys. B, 2023, 32 (**12**): 127401. DOI: 10.1088/1674-1056/ace315

Extremely fast vortex dynamics in $Bi_2Sr_2Ca_2Cu_3O_{10+\delta}$ crystalline nanostrip

A B Yu(于奥博), C T Lin(林成天), X F Zhang(张孝富), and L X You(尤立星)
Chin. Phys. B, 2023, 32 (**6**): 067402. DOI: 10.1088/1674-1056/acb425

Effect of thickness on magnetic properties of single domain GdBCO bulk superconductors

Ping Gao(高平), Wan-Min Yang(杨万民), Ting-Ting Wu(武婷婷), Miao Wang(王妙), and Kun Liu(刘坤)
Chin. Phys. B, 2023, 32 (**2**): 027401. DOI: 10.1088/1674-1056/ac7a13

Conservation of the particle-hole symmetry in the pseudogap state in optimally-doped $Bi_2Sr_2CuO_{6+\delta}$ superconductor

Hongtao Yan(闫宏涛), Qiang Gao(高强), Chunyao Song(宋春尧), Chaohui Yin(殷超辉), Yiwen Chen(陈逸雯), Fengfeng Zhang(张丰丰), Feng Yang(杨峰), Shenjin Zhang(张申金), Qinjun Peng(彭钦军), Guodong Liu(刘国东), Lin Zhao(赵林), Zuyan Xu(许祖彦), and X. J. Zhou(周兴江)
Chin. Phys. B, 2022, 31 (**8**): 087401. DOI: 10.1088/1674-1056/ac7214

RAPID COMMUNICATION

Spin fluctuations and orbital-selective superconductivity in Ba_2CuO_{4-y}: A FLEX study

Pei-Jun Zheng(郑裴俊)[1,2], Ya-Min Quan(全亚民)[1], and Liang-Jian Zou(邹良剑)[1,2,†]

[1] *Key Laboratory of Materials Physics, Institute of Solid State Physics, HFIPS, Chinese Academy of Sciences, Hefei* 230031, *China*
[2] *Science Island Branch of Graduate School, University of Science and Technology of China, Hefei* 230026, *China*

(Received 8 September 2024; revised manuscript received 28 October 2024; accepted manuscript online 30 October 2024)

Recently discovered Ba_2CuO_{4-y} provides new perspectives to the study of high-temperature superconductivity. Whereas, little is known about the spin dynamics of this material. In this work, we employ the fluctuation exchange (FLEX) approximation within the framework of spin-fluctuation mediated superconductivity to examine the behavior of the spin fluctuations of a two-orbital Hubbard model for Ba_2CuO_{4-y}. Our calculations reveal an extraordinary spin resonance mode coupled to the superconducting state in the hole-underdoped regime. Furthermore, we confirm that the coupling between the electrons and this resonance mode can lead to a dip-like feature in the electronic spectrum as a feedback effect. In the hole-overdoped regime, by incorporating self energy into our calculations, we obtain orbital-dependent renormalizations and show how these self-energy effects can lead to the detailed gap structures and the orbital-selective superconductivity, which could not be obtained in a previous study using random phase approximation (RPA). This research may shed new light on searching for unconventional superconductors with higher transition temperatures.

Keywords: fluctuation exchange approximation, spin fluctuation spectrum, spin resonance peak

PACS: 74.72.−h, 71.30.+h, 75.30.Kz, 71.27.+a **DOI:** 10.1088/1674-1056/ad8cbe

1. Introduction

Although nearly four decades have passed since the first superconducting cuprate was discovered, high-temperature superconductivity remains one of the most flourishing research fields in condensed matter physics. Massive efforts have been made to unravel the pairing mechanisms and find effective routes to raise the superconducting transition temperature (T_c), but the mystery of material differences in T_c is still far from completely understood. Recently, a novel kind of cuprate superconductor Ba_2CuO_{4-y} (Ba214) with T_c approximately 73 K was discovered by Jin *et al.*,[1,2] which was believed to be a distinct branch of the high-T_c family[3] because of its unique orbital characteristic. In spite of the same K_2NiF_4 structure as $La_{2-x}Sr_xCuO_4$, Ba214 has a shorter apical Cu–O bond length because of the compressed octahedron,[1] which is in sharp contrast to the previous known cuprate superconductors. Correspondingly, the closer apical oxygen will push up the energy level of the $d_{3z^2-r^2}$ (d_{z^2}) orbital, leading to its contribution to the low-energy electronic states. In consequence, this new cuprate superconductor is a multi-orbital system similar to iron-based superconductors, and multi-orbital models should be used to capture its low-energy physics. Moreover, contrary to the relatively low hole doping in most conventional cuprates, the superconducting state in Ba214 is realized in a heavily hole-overdoped regime with hole doping $x = 2(1-y) = 0.4$, which is reminiscent of previously discovered high-T_c hole-overdoped cuprates.[4–7] Indeed, the possibility of realizing high T_c in highly hole-overdoped cuprates and multi-orbital Hubbard model[8–10] has already been proposed, so that the orbital degree of freedom in newly found cuprate Ba214 deserves further exploration.[11]

Meanwhile, it is well known that multi-orbital character may give rise to various novel phenomena such as orbital-selective Mott transition (OSMT)[12–15] and nematicity,[16–19] the orbital degree of freedom also brings more complexity to superconductivity, allowing more abundant physics like the orbital-selective superconductivity (OSSC)[20–24] and corresponding anisotropic spin excitations[25,26] as well. In multi-orbital Ba214 system, although different crystal structures and models have been suggested and investigated in various theoretical studies,[27–36] little effort has been devoted to the behavior of spin fluctuations. However, as the spin fluctuations carry important information on the nature of magnetism and the characteristics of superconductivity, it is of great value to thoroughly study their behavior in such a novel superconductor, which may contribute to our further understanding of the pairing mechanism underneath the unconventional superconductivity and spark brand new thoughts about raising the critical temperature T_c.

In this sense, the Ba214 system provides an ideal platform to explore how the orbital-related correlations can affect the superconducting gap structure and examine the spin dynamics in both the normal state and the superconducting state. More importantly, it also offers a precious opportunity to un-

†Corresponding author. E-mail: zou@theory.issp.ac.cn
© 2024 Chinese Physical Society and IOP Publishing Ltd

derstand the pairing mechanism in this novel kind of superconductor and serves as an excellent testing ground for finding new ways to raise T_c in unconventional superconductors. With this motivation, in this work we compute the superconducting pairing symmetries and the corresponding gap distributions in the two-orbital Hubbard model of Ba214 using the fluctuation exchange (FLEX) approximation. Compared to the simple random phase approximation (RPA) calculations adopted in Ref. [27], the FLEX formalism can take the feedback effect of self energy into account self-consistently, which naturally makes it possible to describe the OSSC brought by orbital-dependent correlations.[37] Our results reveal that while FLEX can reproduce the major pairing symmetries given by RPA calculations in the same parameter regime, we obtain more detailed gap structures and, furthermore, the orbital-selective gap distributions, which is not possible with simple RPA procedures. In addition, we investigate the behavior of spin excitations with this model. For the first time in this compound, we identify the unambiguous evidence of a spin resonance mode in the superconducting state, and we also establish the relationship between the distribution of spin-fluctuation spectral weight and the hole doping level in the normal state.

The paper is organized as follows. In Section 2, we describe the two-orbital model we used to study the hope-doped Ba_2CuO_{4-y} system and introduce the main procedures of the FLEX approximation approach implemented in both the $T < T_c$ and $T > T_c$ regimes. In Section 3, the numerical results in both the superconducting state and the normal state are presented and discussed. In Subsection 3.1, we study the evolution of the superconducting gap with temperature T, as well as the specific characters of the spin excitations and the quasiparticle excitations distinct in the superconducting state. In Subsection 3.2, we explore the orbital-selective physics and its impact on superconducting pairing. Moreover, we also investigate the evolution of spin excitation spectra when we increase the hole doping level into the highly overdoped regime. Section 4 provides a brief summary of the principal findings and conclusions. Further implications of our results are also discussed.

2. Model Hamiltonian and methods

2.1. Two-orbital Hubbard model

In this paper, we adopt the following two-orbital Hubbard model proposed in Ref. [27], which captures the main features of the band structures near the Fermi surface:

$$H = H_0 + H_{\rm int}, \tag{1}$$

$$H_0(\boldsymbol{k}) = \sum_{\substack{\boldsymbol{k},\sigma\\ \alpha,\beta}} \left\{\xi_{\alpha\beta}(\boldsymbol{k}) + [\varepsilon_\alpha - \mu]\delta_{\alpha\beta}\right\} c^\dagger_{\alpha\sigma}(\boldsymbol{k}) c_{\beta\sigma}(\boldsymbol{k}). \tag{2}$$

Here α and β are orbital indices for two e_g orbitals ($3d_{x^2-y^2}$, $3d_{z^2}$), $\xi_{\alpha\beta}(\boldsymbol{k})$ is the tight-binding Hamiltonian in the orbital space. $c^\dagger_{\alpha\sigma}$ ($c_{\beta\sigma}$) denotes the creation (annihilation) operator of an electron from orbital α (β) and with spin $\sigma =\uparrow(\downarrow)$. ε_α represents the on-site energy of the α orbital and specifically, while $\varepsilon_{d_{x^2-y^2}} = -0.222$ eV keeps as a constant, the energy of orbital d_{z^2} varies with the hole concentration $x = 2(1-y)$ as $\varepsilon_{d_{z^2}} = 0.661 - 5(1-x)$. The chemical potential μ is adjusted by keeping an electron filling $n = 3 - x = 1 + 2y$. $\xi_{\alpha\beta}(\boldsymbol{k})$ is given by

$$\begin{aligned}\xi_{11/22}(\boldsymbol{k}) &= 2t_{11/22}(\cos k_x + \cos k_y) + 4t'_{11/22}\cos k_x \cos k_y \\ &\quad + 2t''_{11/22}(\cos 2k_x + \cos 2k_y), \end{aligned}\tag{3}$$

$$\xi_{12/21}(\boldsymbol{k}) = 2t_{12}(\cos k_x - \cos k_y) + 2t''_{12}(\cos 2k_x - \cos 2k_y), \tag{4}$$

where the model parameters are given in Table 1.

To take account of electron correlation effects, we adopt the on-site multi-orbital electronic interactions as follows:

$$\begin{aligned} H_{\rm int} &= U\sum_{i,\alpha} n_{i\alpha\uparrow}n_{i\alpha\downarrow} + U'\sum_{i,\alpha>\beta} n_{i\alpha}n_{i\beta} \\ &\quad - J\sum_{i,\alpha>\beta,\sigma\sigma'} c^\dagger_{i\alpha\sigma}c_{i\alpha\sigma'}c^\dagger_{i\beta\sigma'}c_{i\beta\sigma} \\ &\quad + J'\sum_{i,\alpha\neq\beta} c^\dagger_{i\alpha\uparrow}c^\dagger_{i\alpha\downarrow}c_{i\beta\downarrow}c_{i\beta\uparrow}, \end{aligned}\tag{5}$$

with intraorbital (U) and interorbital (U') repulsive interactions as well as Hund's coupling (J) and pair hopping (J'). Assuming rotational symmetry for the interaction, these parameters are related by $U' = U - J - J'$ and $J = J'$. Besides, $n_{i\alpha\sigma} = c^\dagger_{i\alpha\sigma}c_{i\alpha\sigma}$ is the occupation number of the orbital α with spin σ at site i and $n_{i\alpha} = \sum_\sigma n_{i\alpha\sigma}$ is the number of total electrons in this orbital.

Table 1. The model parameters of the tight-binding Hamiltonian of Ba_2CuO_{4-y} at half filling in eV, corresponding to the 1st, 2nd and 3rd nearest-neighbor intraorbital and interorbital hoppings. Values of the parameters have been taken from Ref. [27].

	1st (t)	2nd (t')	3rd (t'')
Intraorbital $d_{x^2-y^2}$	$t_{11} = 0.504$	$t'_{11} = -0.067$	$t''_{11} = -0.13$
Intraorbital $d_{3z^2-r^2}$	$t_{22} = -0.196$	$t'_{22} = -0.026$	$t''_{22} = -0.029$
Interorbital	$t_{12} = 0.302$	$t'_{12} = 0$	$t''_{12} = 0.051$

2.2. The fluctuation exchange approximation

The FLEX approximation, introduced by Bickers and Scalapino,[38,39] is based on the conserving approximation.[40,41] It is a convenient tool for dealing with fluctuating many-body electronic systems. As a perturbative diagrammatic method, it sums over the infinite series of bubble terms and ladder terms of the Feynmann diagrams to describe the effective interactions caused by the exchange of spin and charge fluctuations, which play a major role when the system is in the vicinity of a spin or charge instability. Because of its perturbative nature, it can only deal with weak to moderate coupling systems. However, unlike the RPA, it also takes self energy into account so the fermionic propagators

and bosonic response functions are dressed, from which we can obtain renormalized spectral functions and moreover, the orbital-selective physics. In this paper, we use its multi-orbital extension[42,43] to cope with the above two-orbital Hubbard model.

FLEX can be implemented either in the superconducting state or in the normal state. In order to gain further insights into the superconducting properties, we first proceed from the superconducting state. Since there is Cooper pair condensation when $T < T_c$, we should include the anomalous quasiparticle propagator and self energy. Here we follow the notations used in Refs. [44–47], where the basic formalisms and several computational techniques are also discussed. First, we start with the bare normal and anomalous Green's functions in orbital space and on the Matsubara frequency axis: $G_0^{-1}(\boldsymbol{k}, \mathrm{i}\omega_n) = (\mathrm{i}\omega_n + \mu)\mathbb{1} - H_0(\boldsymbol{k})$ and $F_0(\boldsymbol{k}, \mathrm{i}\omega_n) = 0$. And then we calculate the irreducible spin and charge susceptibilities using the following equations:

$$\chi_{s,0}^{l_1l_2l_3l_4}(q) = -\frac{T}{N}\sum_k [G_{l_2l_3}(k+q)G_{l_4l_1}(k) + F_{l_2l_4}(k+q)F^*_{l_3l_1}(k)], \tag{6}$$

$$\chi_{c,0}^{l_1l_2l_3l_4}(q) = -\frac{T}{N}\sum_k [G_{l_2l_3}(k+q)G_{l_4l_1}(k) - F_{l_2l_4}(k+q)F^*_{l_3l_1}(k)], \tag{7}$$

where $\omega_n = (2n+1)\pi T$ and $\nu_n = 2n\pi T$ are fermionic and bosonic Matsubara frequencies. T is the temperature, and N is the number of k points. Note that for simplicity, here we adopt the 4-vector notation so $k = (\boldsymbol{k}, \mathrm{i}\omega_n)$ and $q = (\boldsymbol{q}, \mathrm{i}\nu_n)$ stand jointly for the crystal momentum (or wave vector) and the Matsubara frequencies.

The RPA spin and charge susceptibilities are given by

$$\chi_s(q) = [1 - U^S\chi_{s,0}(q)]^{-1}\chi_{s,0}(q),$$
$$\chi_c(q) = [1 + U^C\chi_{c,0}(q)]^{-1}\chi_{c,0}(q), \tag{8}$$

where the matrix elements of the interaction matrices in the spin (U^S) and charge (U^C) sectors are

$$U^S_{ij,kl} = \begin{cases} U, & \\ U', & \\ J, & \\ J', & \end{cases} \quad U^C_{ij,kl} = \begin{cases} U, & \text{if } i=j=k=l, \\ -U'+2J, & \text{if } i=k\neq j=l, \\ 2U'-J, & \text{if } i=j\neq k=l, \\ J', & \text{if } i=l\neq j=k. \end{cases}$$

In the sense of spin-fluctuation-driven superconductivity, we can obtain the normal and anomalous effective interactions induced by spin and charge fluctuations

$$V_N(q) = \frac{3}{2}U^S\left(\chi_s(q) - \frac{1}{4}\chi_{+,0}(q)\right)U^S + \frac{1}{2}U^C\left(\chi_c(q) - \frac{1}{4}\chi_{+,0}(q)\right)U^C + \frac{1}{2}(3U^S - U^C), \tag{9}$$

$$V_A(q) = \frac{3}{2}U^S\left(\chi_s(q) - \frac{1}{4}\chi_{-,0}(q)\right)U^S - \frac{1}{2}U^C\left(\chi_c(q) + \frac{1}{4}\chi_{-,0}(q)\right)U^C + \frac{1}{2}(U^S + U^C), \tag{10}$$

where $\chi_{\pm,0}(q) = \chi_{s,0}(q) \pm \chi_{c,0}(q)$. Subsequently, the normal and anomalous self energies can be calculated by

$$\Sigma_{lm}(k) = \frac{T}{N}\sum_q\sum_{l',m'} V_N^{ll',mm'}(q)G_{l'm'}(k-q), \tag{11}$$

$$\Phi_{lm}(k) = \frac{T}{N}\sum_q\sum_{l'm'} V_A^{ll',m'm}(q)F_{l'm'}(k-q). \tag{12}$$

Finally, the dressed normal and anomalous Green's functions can be determined by solving the coupled Dyson–Gorkov's equations

$$G(k) = G_0(k) + G_0(k)\Sigma(k)G(k) + G_0(k)\Phi(k)F(k')^*, \tag{13}$$

$$F(k) = G_0(k)\Sigma(k)F(k) - G_0(k)\Phi(k)G(k')^*, \tag{14}$$

where $k' = (-\boldsymbol{k}, \mathrm{i}\omega_n)$. Therefore, Eqs. (6)–(14) can be solved self-consistently to get several important physical quantities.

Above T_c, we can proceed from the normal state with similar procedures.[29,48–51] However, instead of calculating the normal and anomalous self energies self-consistently, we compute the tendency towards superconductivity and pairing symmetry by solving the linearized Eliashberg equation. The detailed process is as follows.

The normal Green's function is self-consistently determined from the Dyson equation

$$G(k)^{-1} = G_0(k)^{-1} - \Sigma(k), \tag{15}$$

where the self energy reads

$$\Sigma_{lm}(k) = \frac{T}{N}\sum_q\sum_{l',m'} \Gamma_{ll',mm'}(q)G_{l'm'}(k-q). \tag{16}$$

The effective interaction consists of contributions from the spin and charge fluctuations as

$$\Gamma(q) = \frac{3}{2}U^S\left[\chi_s(q) - \frac{1}{2}\chi_0(q)\right]U^S + \frac{3}{2}U^S + \frac{1}{2}U^C\left[\chi_c(q) - \frac{1}{2}\chi_0(q)\right]U^C - \frac{1}{2}U^C, \tag{17}$$

with the bare susceptibility given by

$$\chi_0^{l_1l_2l_3l_4}(q) = -\frac{T}{N}\sum_k G_{l_2l_3}(k+q)G_{l_4l_1}(k). \tag{18}$$

The RPA susceptibilities take the same form as in Eq. (8), but the above bare susceptibility χ_0 should be used instead. After the dressed Green's function is obtained, it is plugged into

the following linearized Eliashberg equation with the effective pairing interaction:

$$\lambda\Delta_{\mu\nu}(k) = -\frac{T}{N}\sum_{q,m_i} V^{\mathrm{s/t}}_{\mu m_1 m_4 \nu}(q) G_{m_1 m_2}(k-q) \times \Delta_{m_2 m_3}(k-q) G_{m_4 m_3}(q-k), \quad (19)$$

in which the pairing interactions in spin singlet and triplet states are

$$V^{\mathrm{s}}(q) = \frac{3}{2}U^{\mathrm{S}}\chi_{\mathrm{s}}(q)U^{\mathrm{S}} - \frac{1}{2}U^{\mathrm{C}}\chi_{\mathrm{c}}(q)U^{\mathrm{C}} + \frac{1}{4}(3U^{\mathrm{S}} + U^{\mathrm{C}}), \quad (20)$$

$$V^{\mathrm{t}}(q) = -\frac{1}{2}U^{\mathrm{S}}\chi_{\mathrm{s}}(q)U^{\mathrm{S}} - \frac{1}{2}U^{\mathrm{C}}\chi_{\mathrm{c}}(q)U^{\mathrm{C}} - \frac{1}{4}(U^{\mathrm{S}} - U^{\mathrm{C}}). \quad (21)$$

By solving Eq. (19), we can get several eigenvalues λ and corresponding eigenfunctions $\Delta_{\mu\nu}(k)$, which represent the pairing strengths and pairing gap functions, respectively. When the largest eigenvalue is equal to 1 (i.e., $\lambda = 1$), the system will undergo a superconducting phase transition and the corresponding temperature will be T_{c}. In this sense, $\lambda(T)$ at a fixed temperature can be seen as a measure of the strength of the superconducting instability. The pairing symmetry of the superconducting state is determined from the momentum structure of the corresponding eigenfunction $\Delta(\boldsymbol{k})$.

In actual calculations, we take 64×64 k-mesh in the first Brillouin zone (BZ) and 4096 Matsubara frequencies on the imaginary frequency axis for low temperatures. We have verified that a 128×128 k-point mesh gives essentially the same results. So in order to get finer spin excitation spectra, we use a denser grid in some calculations. In order to obtain the physical quantities in the real frequency regime, the Padé approximation is used for the numerical analytic continuation.[52]

3. Numerical results

In the following, we first calculate the properties of the superconducting state in the hole-underdoped regime $x = 0.15$ and then implement computation from the normal state ($T = 0.007$ eV) in the hole-overdoped regime $x = 0.85$. Here we show the Fermi surfaces of both cases in the normal state in Fig. 1, from which we can see that there are respectively one band and two bands crossing the Fermi level E_{F} in these two cases, forming different Fermi surface topologies.

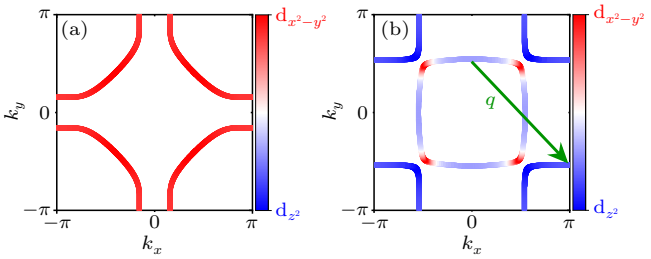


Fig. 1. The bare Fermi surfaces for the (a) hole-underdoped case ($x = 0.15$) and (b) hole-overdoped case ($x = 0.85$). The green arrow in (b) marks the nesting vector $\boldsymbol{q} \approx (\pi, \pi)$ of the two Fermi pockets. In the colorbar, the red color denotes $d_{x^2-y^2}$ orbital and the blue color denotes d_{z^2} orbital.

3.1. Hole-underdoped case and superconducting state properties

Within the scheme of self-consistent FLEX approximation in the superconducting state, we search for stable solutions at the hole doping level $x = 0.15$ and different temperatures. The interaction constants we use are $U = 2.0$ eV and $J = J' = 0.125U$. First, we note that the converged superconducting states are of $d_{x^2-y^2}$-wave symmetry, whose typical energy gap distribution can be seen in the inset of Fig. 2(a). If we further consider its evolution with temperature, we can observe a clear transition from the normal state to the superconducting state near $T = 105$ K. As shown in Fig. 2(a), slightly below this transition temperature T_{c}, the energy gap grows rapidly towards a nearly constant value, which highlights a typical signature of a superconducting transition. We also calculate the spectral function and local density of states through the analytical continuation of the converged Green's function

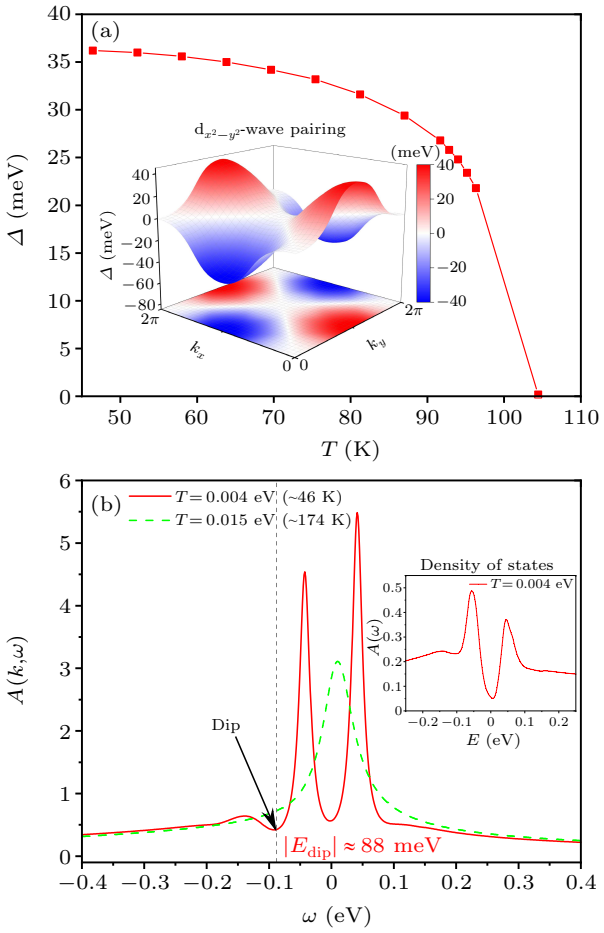


Fig. 2. (a) Temperature dependence of the maximum value of the energy gap. The inset shows the momentum dependence of the self-consistent gap solution at $T = 0.004$ eV (~ 46 K), which clearly characterizes the $d_{x^2-y^2}$-wave pairing structure. (b) The fermionic spectrum $A(\boldsymbol{k}, \omega)$ at a particular $\boldsymbol{k}$ point on the Fermi surface in the superconducting state (solid red line) and the normal state (dashed green line). The black arrow marks the prominent "dip" structure in the superconducting state. The inset displays the local density of states (LDOS) of the band near the Fermi level, which characterizes a V-shaped structure.

using the Padé approximant[52] as

$$A(\boldsymbol{k},\omega) = -\frac{1}{\pi}\mathrm{Im}\left[G(\boldsymbol{k}, \mathrm{i}\omega_n \to \omega + \mathrm{i}\delta)\right],$$

which corresponds to the intensity measured by angle-resolved photoemission spectroscopy (ARPES). As we can see in Fig. 2(b), the fermionic spectrum $A(\boldsymbol{k},\omega)$ in the superconducting state exhibits a remarkable "peak-dip-hump" feature with the dip position located at $|E_{\mathrm{dip}}| \approx 88$ meV. This dip structure was argued to be a strong evidence of the impact on fermions of the coupling between mediating bosonic modes, most likely short-range spin fluctuations, and the electrons.[45] Particularly, it is also believed to be related to the kink feature in the electronic energy dispersion observed by ARPES for cuprates[53] and iron-based superconductors.[54] Moreover, we present the local density of states in the inset of Fig. 2(b), where a prominent V-shaped character suggests a nodal gap structure, which is consistent with $\mathrm{d}_{x^2-y^2}$-wave pairing symmetry. This finding can be validated by future scanning tunneling microscopy (STM) measurements on Ba214.

We further examine the magnetic response in the superconducting state, particularly the dynamical behavior of the spin excitations. From the inset of Fig. 3(a), we can see that the static RPA spin susceptibility $\mathrm{Re}\chi_{\mathrm{s}}(\boldsymbol{q}, \mathrm{i}\omega_n = 0)$ displays a broad peak around the antiferromagnetic wave vector $\boldsymbol{Q}_{\mathrm{AFM}} = (\pi,\pi)$, which suggests that there are strong Néel-type antiferromagnetic spin fluctuations. As to the dynamical properties, it has been observed in cuprates and iron-based superconductors that a sharp resonance peak in the inelastic neutron scattering (INS) experiments was coupled to the onset of superconductivity, and it was recognized as a consequence of the sign-reversing gap structure due to the enhanced coherence factor in the superconducting state.[55] To illustrate this, we present the imaginary part of the dynamical spin susceptibility $\mathrm{Im}\chi_{\mathrm{s}}(\boldsymbol{q},\omega)$ at momentum transfer $\boldsymbol{Q}_{\mathrm{AFM}}$ for three different temperatures in Fig. 3(a). We find that there is only a continuous broad spectrum in the normal state, but the spectral weight gradually concentrates at an intermediate energy range as the temperature approaches T_{c}. When the system enters the superconducting phase, a spin gap opens in the low energy range and a sharp resonance peak develops at a higher energy, as indicated in Fig. 3(a). Specifically, the resonance energy E_{res} at $T = 0.004$ eV is approximately 47 meV. This resonance mode can be analyzed in the spin-1 exciton scenario,[56] where it is accounted for the collective excitations of particle–hole bound states. This excitonic picture naturally leads to an energy threshold of the spin resonance, which is taken as the minimal value of the sum of gap magnitudes on two $\boldsymbol{Q}_{\mathrm{AFM}}$-connected $\boldsymbol{k}$ points of the Fermi surface.[45] Interestingly, as the coupling between electrons and spin fluctuations is believed to mediate unconventional superconductivity, the dip position mentioned above at $|E_{\mathrm{dip}}| \approx 88$ meV is approximately the sum of the resonance energy $E_{\mathrm{res}} \approx 47$ meV and the gap value $|\Delta_{\boldsymbol{k}}|_{\max} \approx 37$ meV. We also analyze the propagating behavior of the resonance mode in energy-momentum space. Figure 3(b) illustrates its dispersion along the direction (q_x,π) in the first BZ, where the major part of the resonance disperses downwards with decreasing intensity when moving away from $\boldsymbol{Q}_{\mathrm{AFM}}$. This pattern, owing to the vanishing gap in the gap nodes of $\mathrm{d}_{x^2-y^2}$-wave pairing symmetry, as explained in Refs. [57,58], may give strong support to the spin-excitonic scenario in spin-fluctuation-mediated superconductivity. Additionally, the upward dispersion at smaller momentum is due to the Umklapp scattering processes, which have much weaker intensity.[58]

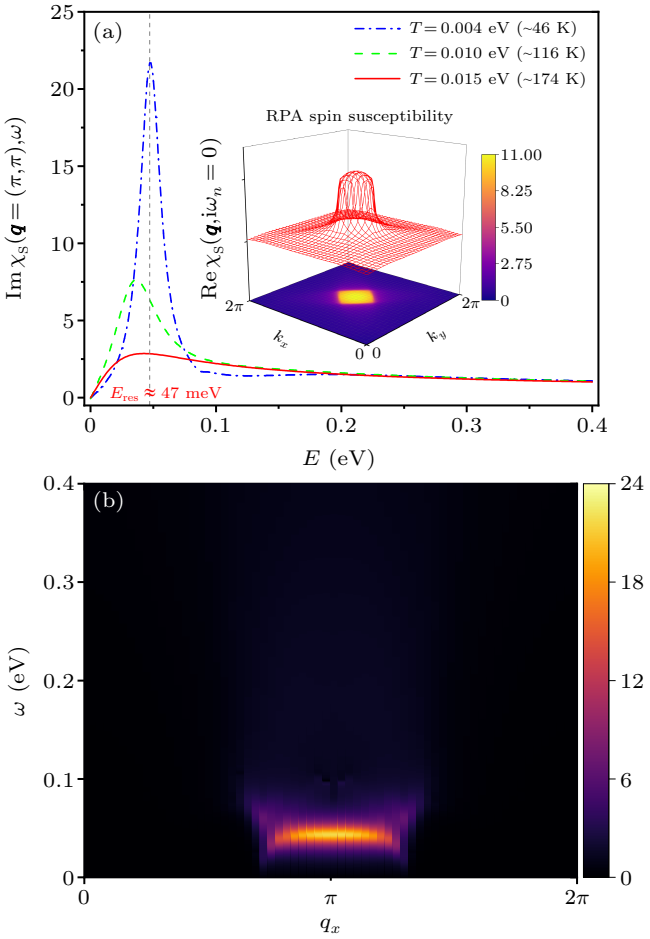


Fig. 3. The spin resonance mode in the superconducting state. (a) The imaginary part of the RPA spin susceptibility $\mathrm{Im}\chi_{\mathrm{s}}(\boldsymbol{q},\omega)$ at $\boldsymbol{Q}_{\mathrm{AFM}} = (\pi,\pi)$ and different temperatures. The inset shows the maximum eigenvalue of the real part of the RPA spin susceptibility at the first Matsubara frequency $\mathrm{Re}\chi_{\mathrm{s}}(\boldsymbol{q}, \mathrm{i}\omega_n = 0)$. (b) The dispersion of the resonance mode along the direction (q_x,π) in the BZ. It corresponds to the result at $T = 0.004$ eV.

3.2. Hole-overdoped case and normal state properties

3.2.1. Pairing eigenvalues and symmetries

In the highly hole-overdoped case, both the $\mathrm{d}_{x^2-y^2}$ orbital and the d_{z^2} orbital contribute to the Fermi surface. In this case, our FLEX calculation did not reach a convergent solution in

the superconducting state, so here we focus on the properties of the normal state. Taking the self-energy effect into account, the quasiparticle bands can be remarkably renormalized under large interactions and they can be estimated by diagonalizing the following matrix:[47]

$$\begin{bmatrix} \xi'_{11}(\boldsymbol{k}) - \mu + \Sigma_{11}(\boldsymbol{k}, \mathrm{i}\pi T) & \xi_{12}(\boldsymbol{k}) + \Sigma_{12}(\boldsymbol{k}, \mathrm{i}\pi T) \\ \xi_{21}(\boldsymbol{k}) + \Sigma_{21}(\boldsymbol{k}, \mathrm{i}\pi T) & \xi'_{22}(\boldsymbol{k}) - \mu + \Sigma_{22}(\boldsymbol{k}, \mathrm{i}\pi T) \end{bmatrix},$$

where $\xi'_{\alpha\alpha}(\boldsymbol{k}) = \xi_{\alpha\alpha}(\boldsymbol{k}) + \varepsilon_\alpha$. $\Sigma_{\alpha\beta}(\boldsymbol{k}, \mathrm{i}\pi T)$ denotes the components of the normal self energy in orbital space and at the first fermionic Matsubara frequency. Since this approximation is more reliable near the Fermi level, we focus on the renormalized Fermi surface as shown in Fig. S1(a) (see supplementary material). Similar to that in Fig. 1(b), there are two pockets at the Fermi level, with the electron pocket centered around the Γ point and the hole pocket centered around the M point. As we increase the hole-doping level towards the half-filling case (i.e., $x = 1.0$), the electron pocket shrinks in size while the hole pocket expands, so they nearly touch each other when $x = 0.95$. Besides, it is worth noting that both pockets are gradually becoming square-shaped in this process.

As a result, the nesting between electron and hole pockets is strongly enhanced, and one can see that the RPA spin susceptibility is more and more commensurate (see Fig. S1(b)), i.e., the peak of the RPA susceptibility is gradually concentrated at the antiferromagnetic wave vector $\boldsymbol{Q}_{\mathrm{AFM}} = (\pi, \pi)$. This enhanced peak in spin susceptibility further induces pronounced antiferromagnetic spin fluctuations in this system, which will finally result in much stronger effective interaction in the interband scattering channel. Moreover, the increasingly perfect nesting condition, as we will see later, has a profound impact on the redistribution of the spectral weights in the spin fluctuation spectrum.

In the formula of the RPA spin susceptibility, the denominator $\left[1 - U^{\mathrm{S}}\chi_0(q)\right]$ should be bigger than zero. Otherwise, there will be errors in the whole calculation. If the denominator approaches zero, the RPA spin susceptibility diverges and the whole system will exhibit spin-density-wave (SDW) instability, where FLEX calculation is prone to convergence problems. Therefore, to illustrate if the system is near the SDW state, here we introduce the static Stoner factor in the spin sector α_{S}[59,60] defined as the largest real part of the eigenvalues of $\left[U^{\mathrm{S}}\chi_0(\boldsymbol{q}, \mathrm{i}\nu_n = 0)\right]$. We calculate α_{S} for different Hund couplings J when increasing U, and the results are shown in Fig. 4(a). As expected, increasing both U and J can enhance the tendency towards the SDW instability, but the effect of increasing U is much more prominent. Increasing Hund's coupling, however, will decrease the maximum U value below which the FLEX algorithm can finally achieve a convergent solution. For example, when $J/U = 0.06$, the maximum value of U we can take is 2.0 eV, while it drops to 1.3 eV when $J/U = 0.18$.

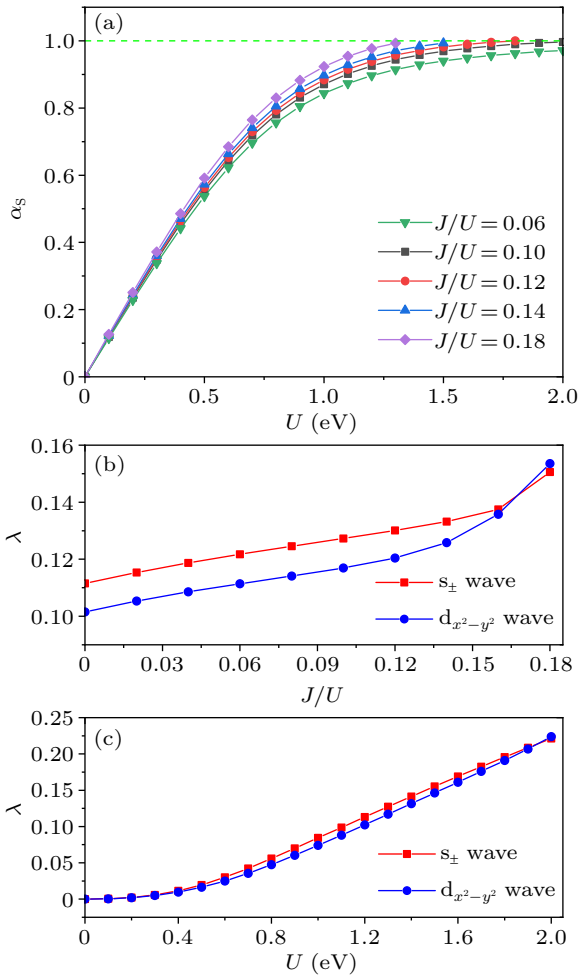


Fig. 4. (a) Spin Stoner factor as the maximum eigenvalue of $\left[U^{\mathrm{S}}\chi_0(\boldsymbol{q}, \mathrm{i}\omega_n = 0)\right]$ calculated for different J/U and U from 0 eV to 2.0 eV, $x = 0.85$ in the hole-overdoped case. The green dashed line marks the boundary of the SDW phase, where the Stoner factor equals 1. (b) and (c) The largest two eigenvalues for the $s_{\pm}$-wave and $d_{x^2-y^2}$-wave pairing symmetries as a function of J/U and U, respectively. In panel (b), we fix $U = 1.3$ eV. In panel (c), we fix $J = 0.10U$.

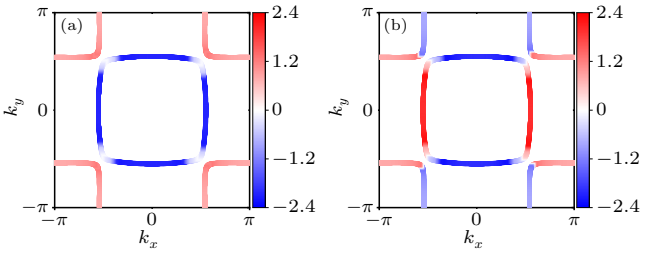


Fig. 5. The first leading two eigenfunctions (i.e., the gap functions) of the linearized Eliashberg equation for $x = 0.85$, both of which are plotted on the bare Fermi surface. The color map from blue to red denotes the sign of the gap value. (a) $s_{\pm}$-wave symmetry; (b) $d_{x^2-y^2}$-wave symmetry.

We have also calculated the largest eigenvalues and the corresponding gap functions under different conditions of U and J. As illustrated in Figs. 4(b) and 4(c), the first two leading eigenfunctions correspond to $s_{\pm}$-wave (A_{1g}) and $d_{x^2-y^2}$-wave (B_{1g}) pairing symmetries, respectively. Meanwhile, in most cases, the pairing eigenvalue of the $s_{\pm}$ wave is slightly bigger than that of the $d_{x^2-y^2}$ wave, except when the whole system gets close to the SDW instability, where $d_{x^2-y^2}$ is de-

generate to $s_{\pm}$ or even dominates. This is a quite interesting feature because the $d_{x^2-y^2}$ wave gap function has nodes on Fermi pockets, as shown in Fig. 5(b), which will cause higher energy in the whole system and thus lower pairing strength under the same condition. We conjecture that the reason for this 'anomaly' lies in the topology of the Fermi surface. Since the FLEX algorithm takes self energy into account, the Fermi surfaces are considerably renormalized when the system is very close to the SDW instability, where the RPA susceptibility is very large because of the nearly-zero Stoner factor. So it is very likely that the Fermi pockets have a larger area of gap nodes in the $s_{\pm}$-wave pairing case than in the $d_{x^2-y^2}$-wave pairing case when the system approaches the boundary of SDW instability, resulting in smaller superconducting condensation energy and thus a smaller pairing eigenvalue.

3.2.2. Orbital-selective gap distributions

Since this model involves two orbitals, it is natural to ask if there are orbital-correlated physics in this unconventional superconductor system. In order to investigate the renormalization effect of self energy on different orbitals, we first calculate the dressed electronic structure along a particular high symmetry path in the first BZ and the density of states (DOS) of two orbitals in the highly hole-overdoped $x = 0.85$ case. In Fig. 6(a), the physical spectral density is compared to the bare band structure obtained by diagonalizing $H_0(\boldsymbol{k})$. As seen, both results exhibit relatively good agreement on the whole, but the former has obvious renormalizations near the high symmetry points. The difference between the renormalized bands and the bare bands can be mainly attributed to the Hartree contribution to the self energy of the electrons, which leads to the energy shift of the bands.[61] This effect may cause non-negligible differences in pairing calculated by the RPA and FLEX methods, since considering the Hartree shift in FLEX can result in qualitatively different spin and charge susceptibilities and thus effective interactions from the ones obtained by using the bare band structure.[47] From Fig. 6(a), we learn that the partially flat band gets closer to the Fermi surface around M, leading to the d_{z^2} orbital contributing more density of states near the Fermi level, as illustrated in Fig. 6(b). This feature, moreover, determines which orbital the pairing strength mainly comes from. To illustrate this, we also calculate the effective pairing strength from different scattering channels and display the results in Fig. 6(c). Since the intraorbital repulsion U in our calculation is the largest coupling constant, we only focus on the intraorbital pairing interactions (i.e., the diagonal components of the pairing vertex) in Fig. 6(c). As expected, if the renormalizations of both orbitals are not very strong, the pairing strength is mainly determined by the DOS around the Fermi surface. Therefore, we can find that the pairing force contributed by spin fluctuations mainly comes from the d_{z^2} orbital and peaks at incommensurate wave vectors $\boldsymbol{Q} = (\pi \pm \delta, \pi \pm \delta)$. This result is similar to that of Ref. [27], which also shows intraorbital scattering from the d_{z^2} orbital dominates the pairing vertex. Qualitatively, this strong intraorbital pairing force will support both $s_{\pm}$-wave and $d_{x^2-y^2}$-wave symmetries according to the Fermi surface topology.

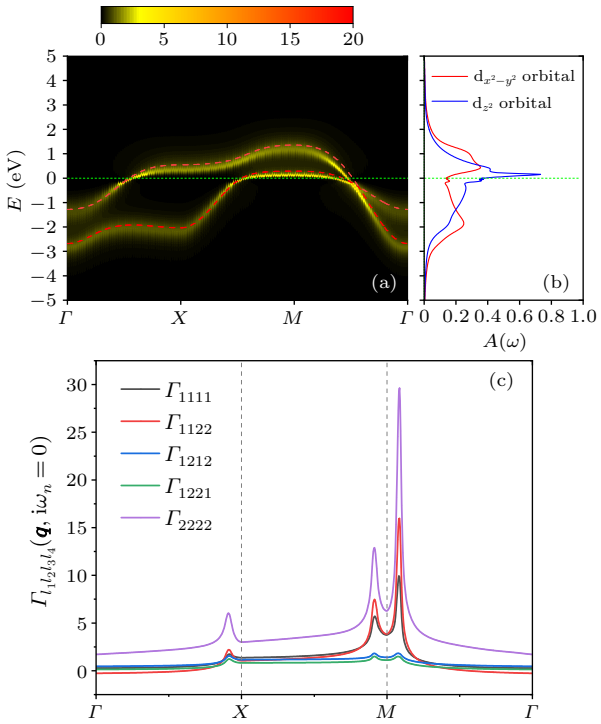


Fig. 6. (a) Single-particle spectral function $A(\boldsymbol{k}, \omega)$ computed at $T = 0.007$ eV for $U = 1.3$ eV and $J = J' = 0.12U$. The red dashed lines indicate bare energy bands along the same high symmetry path. (b) Orbital-projected density of states (DOS) for $d_{x^2-y^2}$ (solid red line) and d_{z^2} orbitals (solid blue line). The short dashed line in green marks the position of the Fermi energy E_F. (c) Orbital-resolved effective pairing strength in singlet pairing channel. Here the subscripts 1 and 2 represent $d_{x^2-y^2}$ and d_{z^2} orbitals, respectively. In panels (a) and (c), the high symmetry points are defined as $\Gamma = (0,0)$, $X = (\pi, 0)$, and $M = (\pi, \pi)$.

However, since the nearest-neighbor hopping of the d_{z^2} orbital is several times smaller than that of the $d_{x^2-y^2}$ orbital, we can expect that the d_{z^2} orbital contains less kinetic energy and thus it is easier to be driven into an insulating state by strong electronic correlations compared to the $d_{x^2-y^2}$ orbital. In the Fermi-liquid regime, an important physical quantity as a measure of the degree of correlation is quasiparticle weight Z, which can be determined by self energy $\Sigma(\boldsymbol{k}, \omega)$. Numerically, it can be approximated by the following equation:[37,62]

$$Z = \left[1 - \frac{\mathrm{d}\mathrm{Re}\Sigma(\boldsymbol{k}, \omega)}{\mathrm{d}\omega}\bigg|_{\omega=0}\right]^{-1} \approx \left[1 - \frac{\mathrm{Im}\Sigma(\boldsymbol{k}, \mathrm{i}\pi T)}{\pi T}\right]^{-1}, \tag{22}$$

using the imaginary part of the self energy at the first Matsubara frequency. The quasiparticle weight of an orbital changes

from $Z = 1$ in the non-interacting limit to $0 < Z < 1$ with increasing interaction strength and completely vanishes in the insulating phase. To illustrate how correlated these two orbitals are in the parameter sets we use, we briefly discuss the behavior of their quasiparticle weights as a function of interaction strength U. The results are displayed in Fig. 7(b) for fixed J/U at $T = 0.007$ eV and as a function of repulsion U. Apparently, with J/U fixed and U increasing, the quasiparticle weights of two orbitals both decrease. However, the quasiparticle weight of the d_{z^2} orbital drops more quickly than that of the $d_{x^2-y^2}$ orbital, which suggests that the former one is more localized even in the weak and intermediate coupling regimes. Particularly, the difference between the two quasiparticle weights gets greater when U becomes bigger, with the ratio $Z_{d_{x^2-y^2}}/Z_{d_{z^2}}$ approaching 2.0 when $U = 1.8$ eV.

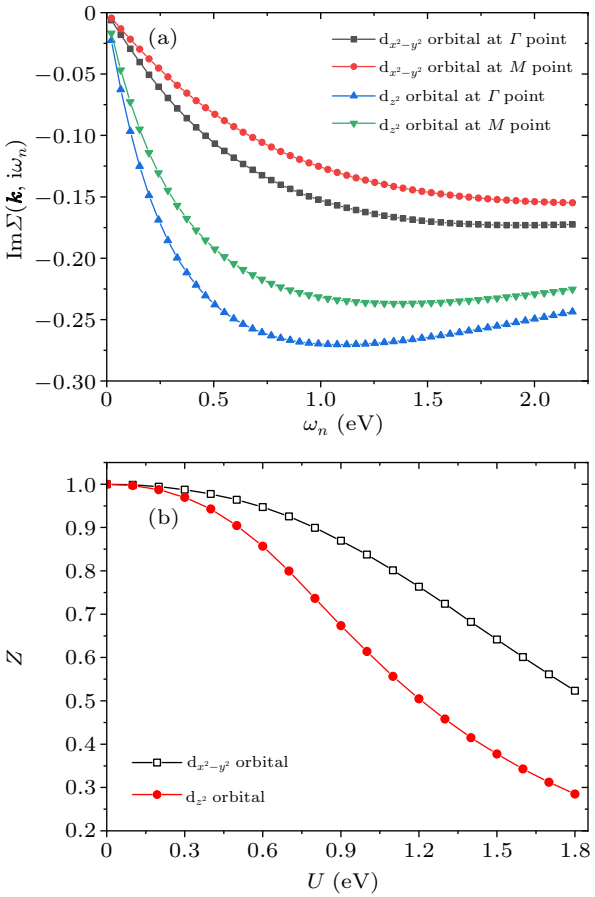


Fig. 7. (a) Imaginary part of the self energy $\mathrm{Im}\Sigma(\boldsymbol{k}, i\omega_n)$ of two orbitals at Γ and M points, respectively. Results are obtained with the interactions $U = 1.3$ eV and $J = J' = 0.12U$. (b) Orbital-resolved quasiparticle weights as a function of interaction U when $J = J' = 0.12U$. Note that here the quasiparticle weights are averaged on both Fermi pockets.

In view of this trend, we can rightfully expect that this system is very likely to undergo an OSMT in a stronger coupling regime, where the d_{z^2} orbital will become completely localized while the $d_{x^2-y^2}$ orbital will still remain itinerant. This was confirmed in a previous study for Ba214 in the half-filled case using the same two-orbital model.[63] However, here the FLEX algorithm fits only to weak to intermediate coupling conditions because of its perturbative nature, so we cannot obtain a concrete OSMP solution.

The dramatic difference between the quasiparticle weights of these two orbitals has a significant influence on the detailed gap distributions, which may lead to orbital-selective pairing. As an illustration of such self-energy feedback effects on the pairing gap structure, in the following, we plot the gap distribution on both electron (α) and hole (β) Fermi pockets as a function of the angle θ defined in Fig. 8(a). Here we first note that the d_{z^2} orbital takes up the most orbital weight on both Fermi pockets, except at the corner of the α pocket, where the $d_{x^2-y^2}$ orbital dominates. Furthermore, from α to β pocket, the orbital weight of the d_{z^2} orbital actually gets larger, as illustrated in Figs. 8(b) and 8(c). Then, in Figs. 8(d) and 8(e), we display the detailed gap structures of $s_\pm$ wave and $d_{x^2-y^2}$ wave on α and β pockets, respectively. It is obvious that the $s_\pm$-wave pairing gap is sign-reversed in different pockets but keeps the sign within each pocket, which is the typical $s_\pm$ wave gap distribution in iron-based superconductors.[44,48,64] And the $d_{x^2-y^2}$-wave pairing gap on both pockets changes its sign in each pocket upon 90° rotation. More importantly, the gap values on the β pocket are definitely smaller than those on the α pocket if we ignore the very small values near the gap nodes.

Combined with the above results, we argue that there is strong evidence for orbital-selective gap distributions in this two-band Hubbard model. Although the quasiparticle weight of the d_{z^2} orbital is much smaller than that of the $d_{x^2-y^2}$ orbital, there are more d_{z^2}-dominated electronic states on the Fermi surfaces and thus provide much stronger pairing strength. Therefore, on the whole, the gap values on the d_{z^2} orbital should be undoubtedly larger, i.e., $\Delta_{d_{z^2}} > \Delta_{d_{x^2-y^2}}$. We have confirmed this in our calculation of the gap function in orbital representation in Fig. S2 (see supplementary material). It is also worth mentioning that we find gap distributions with much smaller anisotropy in momentum space, especially for $s_\pm$-wave pairing, in contrast to that obtained through RPA-based traditional spin-fluctuation calculations done in a previous study.[27] Also, our findings about different "gap details" on both pockets and orbitals were not discovered in their results. Besides, we also notice that two recent RPA studies based on a different crystal structure gave d_{xy} wave pairing symmetry in $Ba_2CuO_{3.25}$[35] and observed a transition of the superconducting pairing symmetry from singlet to triplet while increasing the hole doping.[36] Despite using a multi-orbital model, their results are more about different nesting conditions of the Fermi surfaces rather than orbital-selective physics. However, with the self energy being self-consistently included in our FLEX calculation, we can naturally incorporate orbital-resolved correlations into the pair-

ing vertex and thus gap solutions of the linearized Eliashberg equation (Eq. (19)), giving more realistic results. Therefore, we anticipate that our results of the detailed band-resolved gap distributions and the d_{z^2}-orbital dominant Cooper pairing can be verified by future experimental observations with much higher precision.

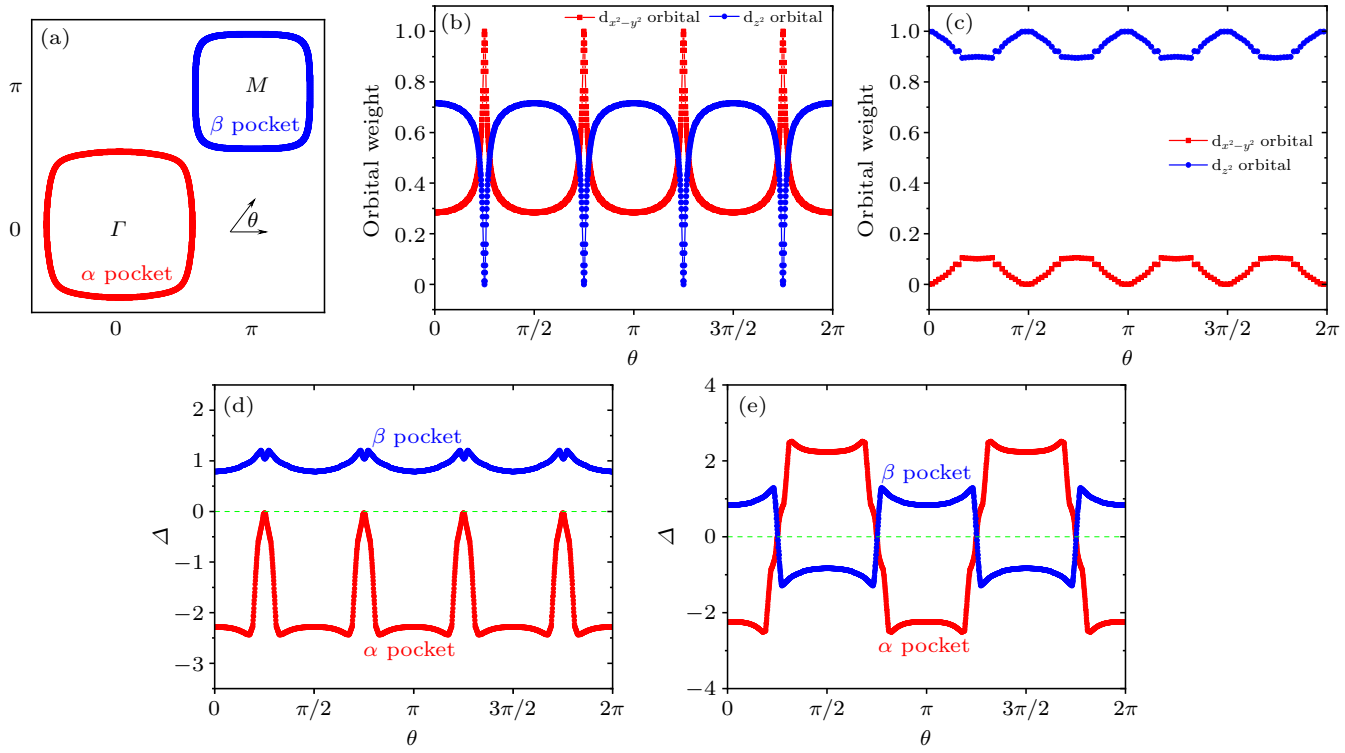


Fig. 8. (a) Normal state Fermi surface at $x = 0.85$. (b) and (c) Distribution of orbital weights along the electron pocket centered at Γ and the hole pocket centered at M, respectively. The red lines represent the $d_{x^2-y^2}$ orbital, while the blue ones represent the d_{z^2} orbital. (d) and (e) Pairing energy gaps as a function of angle θ defined in panel (a) along the two Fermi surfaces around Γ (red) and M (blue), representing $s_{\pm}$-wave and $d_{x^2-y^2}$-wave pairing symmetries, respectively. The interaction parameters are $U = 1.3$ eV and $J = J' = 0.12U$.

3.2.3. Spin excitation spectra

The spin excitation spectra in the normal state reflect the dynamical properties of the pairing glue in the system. Here, we discuss the structure of the spin excitations, $\mathrm{Im}\chi_s(\boldsymbol{q}, \omega)$, along a high symmetry path in the direction (q_x, π) and at different hole-doping levels from $x = 0.80$ to $x = 0.95$, which is displayed in Fig. 9(a). Under the same color intensity scale, we notice that when $x = 0.80$, the spin excitations appear quite weak and almost featureless on the frequency axis, indicating a relatively trivial distribution of the spectral weights of spin fluctuations. However, when we increase the hole-doping level, our results show a maximum in a finite energy range at the momentum transfer $\boldsymbol{Q}_{\mathrm{AFM}} = (\pi, \pi)$. Furthermore, there are two incommensurate peaks located at $\boldsymbol{Q} = (\pi \pm \delta, \pi)$ ($\delta < 0.2\pi$) when $x = 0.80$, but they gradually merge together to form a commensurate peak around $\boldsymbol{Q}_{\mathrm{AFM}}$. More importantly, the spectral weight of the low energy spin fluctuations becomes more and more prominent, which means that the spin excitations in the low energy region dominate the dynamical properties. This behavior is linked to the corresponding changes in the Fermi-surface nesting condition. As the hole doping leads to the shrinking of the electron sheet and the expansion of the hole sheet, the nesting between these two sheets becomes more perfect so that most particle–hole excitations at $\boldsymbol{Q}_{\mathrm{AFM}}$ can arise with very small energy transfer. Therefore, the corresponding spectral weight moves to a lower energy regime. Similarly, this characteristic can also be observed in the low-energy spin fluctuation spectrum. To demonstrate this, we take a series of energy cuts in the low-energy region $\omega \leq 0.1$ eV on the dispersions of spin excitations along the same direction. What we can find is that the low-energy spin fluctuations definitely get larger when the system is close to half filling, as shown in Fig. 9(b). This increasing low-energy spectral weight of spin fluctuations may enhance the renormalization effects of related orbitals, giving rise to the non-Fermi liquid behavior[65] in the normal state, and is also detrimental to superconductivity because of its pairing-breaking nature.[66]

Finally, we discuss the evolution of the spin fluctuations at $\boldsymbol{Q}_{\mathrm{AFM}}$ when lowering the temperature in the normal state. In Fig. 10, we find that a hump structure is obtained when $T = 0.02$ eV (~ 230 K). While decreasing T does not change much the spectral weight of high-energy spin excitations, it gradually modifies the spectral weight in the low-energy region, with those under $\omega \leq 0.1$ eV suppressed and shifted to $\omega \geq 0.1$ eV. This makes the hump structure at $\omega \leq 0.3$ eV

narrower and taller. Particularly, at much lower temperature $T = 0.008$ eV (~ 90 K), the spectral weight is concentrated in a finite energy range ($0.1\ \text{eV} < \omega < 0.15\ \text{eV}$), forming a peak-like structure which is similar to the precursor of the spin resonance peak.

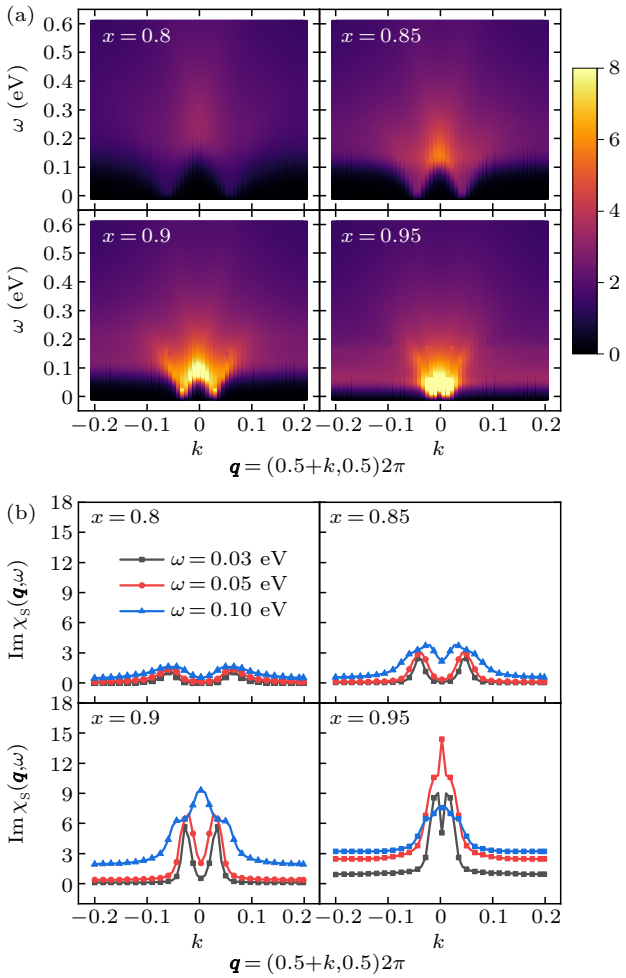


Fig. 9. (a) Imaginary part of $\chi_s(\boldsymbol{q}, \omega)$ along the direction (q_x, π) at different hole-doping levels: $x = 0.80$, $x = 0.85$, $x = 0.90$ and $x = 0.95$. Note that the spectra are plotted using the same color intensity. (b) The corresponding low-energy spin fluctuations along three different energy cuts: $\omega = 0.03$ eV, $\omega = 0.05$ eV and $\omega = 0.10$ eV. The interaction parameters used here are $U = 1.3$ eV and $J = J' = 0.12U$.

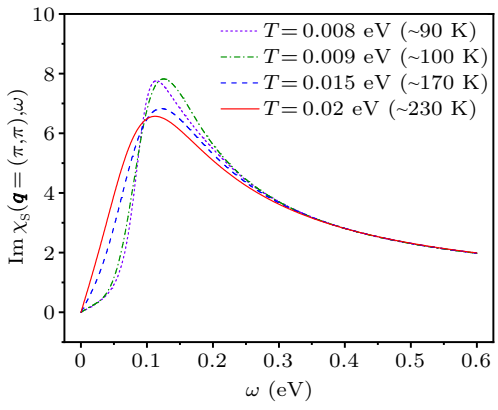


Fig. 10. Evolutions of spin fluctuation spectrum at $\boldsymbol{Q}_{\text{AFM}} = (\pi, \pi)$ with decreasing temperature. The interaction parameters we used here are $U = 1.5$ eV and $J/U = 0.125$ and the hole-doping level is $x = 0.85$.

4. Discussion and conclusion

The discovery of superconductivity in Ba_2CuO_{4-y} at $T_c = 73$ K with anomalously compressed octahedron and considerably high hole doping levels opens up a new possibility in the search for unconventional superconductors with higher transition temperatures. Compared to conventional cuprates, it contains multiple Fermi surfaces so that more scattering channels such as interband scattering are possible, which leads to more diverse pairing symmetries. In this model, Ba214 exhibits $s_{\pm}$-wave pairing similar to that in multiband iron-based superconductors[44,48] in the heavily hole-doped region ($x = 0.85$ as illustrated in Fig. 5(a)), with gap nodes mostly situated between two Fermi pockets. On the other hand, orbital-selective physics such as OSMP could arise from this multi-orbital nature, which indicates remarkably different correlations in these two orbitals. This lays the foundations of OSSC, where electrons in different orbitals combine to form Cooper pairs with different energy gaps, leading to the anisotropic gap structure on the Fermi surfaces. Meanwhile, this anisotropic pairing implies that spin excitations may be orbital selective as well. In fact, we find that spin fluctuations are mostly contributed by the d_{z^2} orbital, as shown in Fig. S3 (see supplementary material), which is compatible with the much bigger orbital-resolved pairing vertex of this orbital mentioned above (Fig. 6(c)) within the FLEX scheme.

More notably, it has been found that doping a large amount of holes can greatly lift T_c,[6] which may be attributed to the multi-orbital nature of the superconductors. Hypothetically, it is suggested that this multi-orbital nature highlights the possibility of an orbital-dependent superconductivity scenario,[63] where electrons in more correlated orbitals provide major contributions to the spin fluctuations and thus superconducting pairing forces, while electrons in less correlated orbitals supply a sufficient density of carriers to form Cooper pairs and increase superfluid density. In this way, the dilemma of having electrons from the same orbital simultaneously play the above two important roles can be avoided and thus may effectively enhance superconductivity. However, the validity of this scenario remains to be confirmed.

On the contrary, in our FLEX calculations, large energy gaps are often accompanied by strong spin fluctuations and pairing forces. In other words, our findings cannot give a clear distinction between the dual roles of electrons. Nevertheless, such high T_c in this system can still be properly explained in this itinerant picture. Intuitively, T_c can be lifted by increasing spin-fluctuation spectral weight and thus enhancing effective pairing interactions. From a Fermi-surface nesting point of view,[67,68] this can be realized by a better nesting condition of the Fermi surfaces. However, excessive concentrations of spectral weights near the Fermi level can also lead to an increased renormalization effect, inducing incoherent electron

scattering, which actually results in a decrease in the pairing strength. This can be more significant for those orbitals with a much narrower bandwidth. On the other hand, the poor Fermi surface nesting would suppress spin fluctuations in the low energy range, thus reducing the pairing interactions, which is also detrimental to superconductivity. Therefore, it is suggested that appropriate Fermi surface nesting and spin fluctuations whose spectral weights are concentrated in a reasonable energy range are most favorable for superconductivity.[10,25] In this system, we find that the pairing interaction is considerably enhanced by the partially flat band near the M point because of the concentrated DOS near the Fermi level. Moreover, as the doping level is far away from the half-filling case, the nesting is degraded to some extent so that the pair-breaking spin fluctuations only take up minor spectral weight. It is therefore possible for such a system to have a relatively high T_c.

In conclusion, by implementing the spin-fluctuation-based FLEX approximation in the two-orbital Hubbard model of Ba214, we have studied its pairing symmetry, gap structure, and spin dynamics in both the superconducting state and the normal state. In the hole-underdoped regime ($x = 0.15$), our results about the spin excitations and quasiparticle excitations reveal a remarkable spin resonance mode and a dip-like feature, respectively, which strongly signifies the coupling between the spin fluctuations and the electrons. In the highly hole-overdoped regime ($x = 0.85$), by incorporating orbital-dependent correlations self-consistently, we obtain orbital-selective superconductivity where the d_{z^2} orbital dominates the Cooper pairing. Moreover, our investigations about the spin dynamics demonstrate much more enhanced low-energy spin fluctuations in the highly hole-overdoped regime close to half filling, which may have negative effects on the Cooper pairing. Although further research is needed to reach a comprehensive understanding of this novel superconductor, our results may serve as a reference for future experimental investigations, especially INS measurements on high-quality samples of single crystals. Hopefully, we believe that the same treatments can also be applied to the similar hole-overdoped Sr_2CuO_{4-y} superconductor,[4,5,69] and we anticipate more exciting findings from future studies on this material.

Acknowledgments

Project supported by the National Natural Science Foundation of China (Grant Nos. 11774350, 11974354, and 11534010). The calculations were performed in the Center for Computational Science of CASHIPS, and partly using a Tianhe-2JK computing time award at the Beijing Computational Science Research Center (CSRC).

References

[1] Li W M, Zhao J F, Cao L P, Hu Z, Huang Q Z, Wang X C, Liu Y, Zhao G Q, Zhang J, Liu Q Q, Yu R Z, Long Y W, Wu H, Lin H J, Chen C T, Li Z, Gong Z Z, Guguchia Z, Kim J S, Stewart G R, Uemura Y J, Uchida S and Jin C Q 2019 *Proc. Natl. Acad. Sci. USA* **116** 12156
[2] Li W, Zhao J and Jin C 2023 *Phys. C* **615** 1354373
[3] Scalapino D J 2019 *Proc. Natl. Acad. Sci. USA* **116** 12129
[4] Liu Q Q, Yang H, Qin X M, Yu Y, Yang L X, Li F Y, Yu R C, Jin C Q and Uchida S 2006 *Phys. Rev. B* **74** 100506
[5] Geballe T and Marezio M 2009 *Phys. C* **469** 680
[6] Gauzzi A, Klein Y, Nisula M, Karppinen M, Biswas P K, Saadaoui H, Morenzoni E, Manuel P, Khalyavin D, Marezio M and Geballe T H 2016 *Phys. Rev. B* **94** 180509
[7] Jiang K, Wu X, Hu J and Wang Z 2018 *Phys. Rev. Lett.* **121** 227002
[8] Sakakibara H, Usui H, Kuroki K, Arita R and Aoki H 2010 *Phys. Rev. Lett.* **105** 057003
[9] Maier T A and Scalapino D J 2011 *Phys. Rev. B* **84** 180513
[10] Nakata M, Ogura D, Usui H and Kuroki K 2017 *Phys. Rev. B* **95** 214509
[11] Oleś A M, Wohlfeld K and Khaliullin G 2019 *Condens. Matter* **4** 46
[12] Anisimov V, Nekrasov I, Kondakov D, Rice T and Sigrist M 2002 *Eur. Phys. J. B* **25** 191
[13] Yi M, Lu D H, Yu R, Riggs S C, Chu J H, Lv B, Liu Z K, Lu M, Cui Y T, Hashimoto M, Mo S K, Hussain Z, Chu C W, Fisher I R, Si Q and Shen Z X 2013 *Phys. Rev. Lett.* **110** 067003
[14] Yu R and Si Q 2013 *Phys. Rev. Lett.* **110** 146402
[15] Quan Y M, Liu D Y, Lin H Q and Zou L J 2018 *J. Magn. Magn. Mater.* **456** 329
[16] Kasahara S, Shi H J, Hashimoto K, Tonegawa S, Mizukami Y, Shibauchi T, Sugimoto K, Fukuda T, Terashima T, Nevidomskyy A H and Matsuda Y 2012 *Nature* **486** 382
[17] Fernandes R M, Chubukov A V and Schmalian J 2014 *Nat. Phys.* **10** 97
[18] Watson M D, Kim T K, Haghighirad A A, Davies N R, McCollam A, Narayanan A, Blake S F, Chen Y L, Ghannadzadeh S, Schofield A J, Hoesch M, Meingast C, Wolf T and Coldea A I 2015 *Phys. Rev. B* **91** 155106
[19] Zheng X J, Huang Z B, Liu D Y and Zou L J 2015 *Phys. Rev. B* **92** 085109
[20] Lu F, Wang W H, Liu D Y, Wang C Z and Zou L J 2010 *J. Phys.: Condens. Matter* **22** 355603
[21] Zhang Y, Lee J J, Moore R G, Li W, Yi M, Hashimoto M, Lu D H, Devereaux T P, Lee D H and Shen Z X 2016 *Phys. Rev. Lett.* **117** 117001
[22] Xu H C, Niu X H, Xu D F, Jiang J, Yao Q, Chen Q Y, Song Q, Abdel-Hafiez M, Chareev D A, Vasiliev A N, Wang Q S, Wo H L, Zhao J, Peng R and Feng D L 2016 *Phys. Rev. Lett.* **117** 157003
[23] Sprau P O, Kostin A, Kreisel A, Böhmer A E, Taufour V, Canfield P C, Mukherjee S, Hirschfeld P J, Andersen B M and Davis J C S 2017 *Science* **357** 75
[24] Liu C, Kreisel A, Zhong S, Li Y, Andersen B M, Hirschfeld P and Wang J 2022 *Nano Lett.* **22** 3245
[25] Li Y, Yin Z, Wang X, Tam D W, Abernathy D L, Podlesnyak A, Zhang C, Wang M, Xing L, Jin C, Haule K, Kotliar G, Maier T A and Dai P 2016 *Phys. Rev. Lett.* **116** 247001
[26] Tian L, Liu P, Xu Z, Li Y, Lu Z, Walker H C, Stuhr U, Tan G, Lu X and Dai P 2019 *Phys. Rev. B* **100** 134509
[27] Maier T, Berlijn T and Scalapino D J 2019 *Phys. Rev. B* **99** 224515
[28] Wang Z, Zhou S, Chen W and Zhang F C 2020 *Phys. Rev. B* **101** 180509
[29] Yamazaki K, Ochi M, Ogura D, Kuroki K, Eisaki H, Uchida S and Aoki H 2020 *Phys. Rev. Res.* **2** 033356
[30] Jiang K, Le C, Li Y, Qin S, Wang Z, Zhang F and Hu J 2021 *Phys. Rev. B* **103** 045108
[31] Zegrodnik M, Wójcik P and Spałek J 2021 *Phys. Rev. B* **103** 144511
[32] Klett M, Schwemmer T, Wolf S, Wu X, Riegler D, Dittmaier A, Di Sante D, Li G, Hanke W, Rachel S and Thomale R 2021 *Phys. Rev. B* **104** L100502
[33] Bai X C, Quan Y M, Lin H Q and Zou L J 2022 *Phys. Rev. B* **105** 184506
[34] Worm P, Kitatani M, Tomczak J M, Si L and Held K 2022 *Phys. Rev. B* **105** 085110
[35] Adhikary P, Gupta M, Chauhan A, Satpathy S, Mukherjee S and Nanda B R K 2024 *Phys. Rev. B* **109** L020505

[36] Adhikary P, Gupta M, Nanda B R K and Mukherjee S 2024 *Phys. Rev. B* **109** 224503
[37] Björnson K, Kreisel A, Rømer A T and Andersen B M 2021 *Phys. Rev. B* **103** 024508
[38] Bickers N E, Scalapino D J and White S R 1989 *Phys. Rev. Lett.* **62** 961
[39] Bickers N and Scalapino D 1989 *Ann. Phys.* **193** 206
[40] Baym G and Kadanoff L P 1961 *Phys. Rev.* **124** 287
[41] Baym G 1962 *Phys. Rev.* **127** 1391
[42] Takimoto T, Hotta T and Ueda K 2004 *Phys. Rev. B* **69** 104504
[43] Kubo K 2007 *Phys. Rev. B* **75** 224509
[44] Zhang J, Sknepnek R, Fernandes R M and Schmalian J 2009 *Phys. Rev. B* **79** 220502
[45] Zhang J, Sknepnek R and Schmalian J 2010 *Phys. Rev. B* **82** 134527
[46] Nocera A, Wang Y, Patel N D, Alvarez G, Maier T A, Dagotto E and Johnston S 2018 *Phys. Rev. B* **97** 195156
[47] Rademaker L, Alvarez-Suchini G, Nakatsukasa K, Wang Y and Johnston S 2021 *Phys. Rev. B* **103** 144504
[48] Sknepnek R, Samolyuk G, Lee Y b and Schmalian J 2009 *Phys. Rev. B* **79** 054511
[49] Yu S L, Kang J and Li J X 2009 *Phys. Rev. B* **79** 064517
[50] Ikeda H, Arita R and Kuneš J 2010 *Phys. Rev. B* **82** 024508
[51] Witt N, van Loon E G C P, Nomoto T, Arita R and Wehling T O 2021 *Phys. Rev. B* **103** 205148
[52] Vidberg H J and Serene J W 1977 *J. Low Temp. Phys.* **29** 179
[53] Abanov A and Chubukov A V 1999 *Phys. Rev. Lett.* **83** 1652
[54] Richard P, Sato T, Nakayama K, Souma S, Takahashi T, Xu Y M, Chen G F, Luo J L, Wang N L and Ding H 2009 *Phys. Rev. Lett.* **102** 047003
[55] Scalapino D J 2012 *Rev. Mod. Phys.* **84** 1383
[56] Eschrig M 2006 *Adv. Phys.* **55** 47
[57] Song Y, Wang W, S Van Dyke J, Pouse N, Ran S, Yazici D, Schneidewind A, Čermák P, Qiu Y, Maple M B, Morr D K and Dai P 2020 *Commun. Phys.* **3** 98
[58] Eremin I, Morr D K, Chubukov A V, Bennemann K H and Norman M R 2005 *Phys. Rev. Lett.* **94** 147001
[59] Takeuchi L, Yamakawa Y and Kontani H 2018 *Phys. Rev. B* **98** 165143
[60] Hiroshi Kontani Rina Tazai Y Y and Onari S 2021 *Adv. Phys.* **70** 355
[61] Karakuzu S, Johnston S and Maier T A 2021 *Phys. Rev. B* **104** 245109
[62] Ikeda H, Arita R and Kuneš J 2010 *Phys. Rev. B* **81** 054502
[63] Ni Y, Quan Y M, Liu J, Song Y and Zou L J 2021 *Phys. Rev. B* **103** 214510
[64] Yao Z J, Li J X and Wang Z D 2009 *New J. Phys.* **11** 025009
[65] Dai Y M, Miao H, Xing L Y, Wang X C, Wang P S, Xiao H, Qian T, Richard P, Qiu X G, Yu W, Jin C Q, Wang Z, Johnson P D, Homes C C and Ding H 2015 *Phys. Rev. X* **5** 031035
[66] Matsumoto K, Ogura D and Kuroki K 2020 *J. Phys. Soc. Jpn.* **89** 044709
[67] Hirschfeld P J, Korshunov M M and Mazin I I 2011 *Rep. Prog. Phys.* **74** 124508
[68] Chubukov A 2012 *Annu. Rev. Condens. Phys.* **3** 57
[69] Hiroi Z, Takano M, Azuma M and Takeda Y 1993 *Nature* **364** 315